Heterogenized molecular (pre)catalysts for water oxidation and oxygen reduction

Ham, C.J.M. van der

2 | Structure dependence on the activation of molecular iridium precatalysts for the water oxidation reaction

Water oxidation using Ir-based complexes is a well-established electrochemical reaction. However, the carbon backbone of the iridium complex is often oxidized under catalytic circumstances yielding ill-defined active species. In this work, a comparison is made between two similar pyridyl-triazolylidene iridium complexes for their electrochemical water oxidation behavior. The proton in the IrL_1L_2 is replaced by a methoxy moiety in IrL_1L_3. The activation behavior of iridium pyridyl-triazolylidene complexes with a Cp^* ligand is highly dependent on the substituents on the triazolylidene ring. Molecular complexes adsorbed on the working electrode are responsible for the water oxidation activity, whilst at the same time part of the ligand backbone is oxidized to carbon dioxide. The active species of both complexes are compared to benchmark systems. The ligands of the active species are partially oxidized but the catalysts still have a molecular nature.

"Miracles are not contrary to nature but only contrary to what we know about nature. "
St. Augustine

Submitted

2.1 Introduction

One of the challenges in the water oxidation reaction mediated by molecular catalysts is the determination which reaction intermediates are present and involved in the catalytic reaction. Mechanistic studies on water oxidation catalysts are typically carried out using sacrificial reagents such as sodium periodate or cerium ammonium nitrate. The use of sacrificial reagents to pinpoint the presence of reaction intermediates in particular has been successful in the case of the relatively robust ruthenium-based molecular catalysts.[1–5]

Studies with sacrificial reagents to pinpoint which reaction intermediates are present during catalysis typically have been less successful with iridium-based catalysts equipped with a pentamethylcyclopentadienyl ligand (Cp^{*-}), in particular since such iridium Cp* complexes typically are precursors rather than the true active species. While keeping the drawbacks of sacrificial oxidants discussed above in mind, the use of a chemical oxidant can be very useful in the isolation of catalytic intermediates, or to detect species that are en route to the catalytically active species. The group of Macchioni discovered that the Cp^{*-} ligand in a $[Cp^*Ir(bzpy)NO_3]$ complex (bzpy = 2-benzoylpyridine) is slowly oxidized in presence of sacrificial reagents in a 1:1 mixtures of acetone and water.[6] They used H_2O_2, cerium ammonium nitrate and $NaIO_4$ as oxidants and found three different species wherein the Cp* ligand has been partially oxidized. Based on the structures that Macchioni *et al.* have observed with NMR spectroscopy (Figure 2.1) it is believed that the first step in catalyst activation is the epoxidation of a Cp* C-C bond of Cp* via an Ir-oxo species. This species is further oxidized by addition of water to the epoxide species. The last intermediate that was detected in this catalyst activation study contains one ketone-moiety on

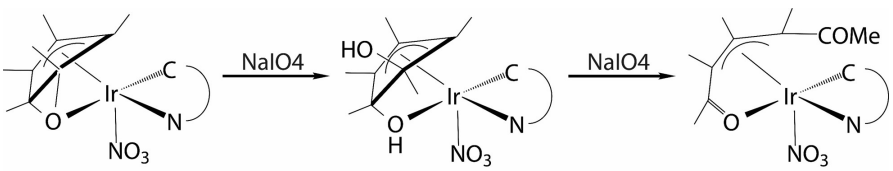

Figure 2.1: Oxidation of petnamethylcyclopentadienyl (Cp*) oxidation at a $[Cp^*Ir(bzpy)NO_3]$ complex upon treatment by periodate as chemical oxidant. Figure reporduced from [6].

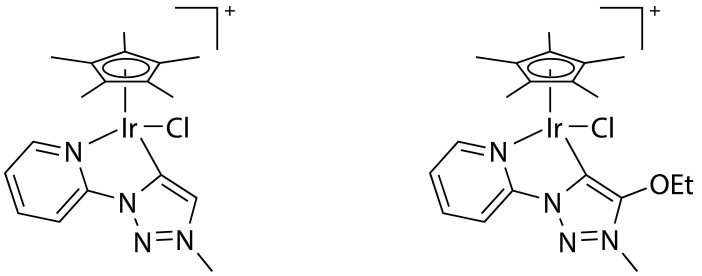

Figure 2.2: The structure of the complexes **1** and **2**.

the ring-opened aromatic remnant of Cp*, of which one is presumably coordinated to the Ir^{III} center. Further oxidation leads to the formation of acetic acid.

The complementary ligands present at iridium appear to be retained during at least the initial stages of catalysis. In the group of Albrecht, a wide variety of pyridyl-triazolylidene and other iridium complexes have been investigated for water oxidation using chemical oxidants to establish a structure-reactivity correlation.[7–13] Two catalysts that are particularly interesting in terms of activity are shown in Figure 2.2 and contain either an unmodified triazolylidene (complex **1**) or an ethoxy substituted triazolylidene ring (complex **2**). Upon treatment of these complexes with chemical oxidants, the rate of oxygen production increases over time, indicating that the catalysts need to be activated before water oxidation can take place. The results with cerium ammonium nitrate show that complex **2** activates more rapidly than complex **1**, which is attributed to the favorable electronic properties of complex **2**.[13] Furthermore both the maximum turnover number and turnover frequency seems to be limited by the amount of cerium present in solution and not by the maximum activity of the complexes.

The use of cerium ammonium nitrate as a sacrificial reagent is not ideal as it could interfere in the catalytic cycle. For example it has been reported that oxygen atom transfer can take place from the coordination sphere of cerium or periodate.[14–16] It has also been observed that cerium can participate in the catalytic cycle by direct coordination to the M-O bond.[17] Moreover it was shown that cerium can be incorporated in the *in situ* formed cataytic nanoparticles during water oxidation catalysis.[18] In light of the possible involvement of sacrificial reagents in this chapter electrochemical techniques are used to study the water oxidation reaction in pres-

ence of **1** and **2**. Such electrochemical tools provide reaction conditions that are much closer to an actual application in a electrochemical or photoelectrochemical water splitting device. In literature a few studies regarding iridium-based water oxidation catalysts have been reported wherein electrochemistry is combined with both *in situ* and *ex situ* techniques to investigate the nature of the catalytic systems. [19–24]

The complex $[Ir(Cp^*)(OH_2)_3]SO_4$ (**3**) has been investigated extensively using both chemical and electrochemical methods. Oxygen evolution starts at the moment that cerium ammonium nitrate is added to the solution containing **3**, indicating that the formation of an active species is extremely fast. An initial turnover frequency of 10.4 min^{-1} is observed with a 5 μM solution of **3** and 78 mM cerium ammonium nitrate at pH 0.89. The turnover frequency increases with catalyst concentration, indicating higher order reaction kinetics for **3**.[19]

Upon electrochemical oxidation of **3** at a graphite electrode in 0.1 M KNO_3 at pH 2.9, a catalytic wave is observed starting at 1.27 V *versus* RHE in the first scan of the cyclic voltammogram.[20] Upon repetitive cycling, a reversible peak redox couple grows at 1.05 V *versus* RHE, with a ΔE of 0.25 mV, which points to an adsorbed redox-active species. This absorbed material consists of amorphous iridium oxide and is called the blue layer. The increase in peak current with each consecutive scan is an indication that more material is deposited onto the working electrode during each scan. With the increase in peak current of the redox couple, the maximum current of the catalytic wave increases as well. After 10 cycles of cyclic voltammetry, 4.1 nmol cm^{-2} iridium is adsorbed as determined by the integration of the redox waves. Upon transfer of the deposited blue layer to a solution deprived of **3**, both the reversible redox couple and the catalytic wave are visible without a decrease in current. By measuring the mass increase using an electrochemical quartz crystal microbalance (EQCM), a total mass increase of 800 ng is observed over four consecutive scans. This suggests that in case of the formation of pure IrO_2, the total amount of electroactive iridium is 5.5%, whereas the remainder of the material is dormant.[21]

In contrast to **3**, which degrades to heterogeneous iridium oxide, the complex $[IrCp^*(pyalc)CF_3COO]$ (**4**, pyalc = 2-(2-pyridyl)-2-propanolate) was shown to produce a well-defined molecular catalyst for the water oxidation reaction.[21] Water oxidation was observed above 1.4 V *versus* RHE at pH 7 at a basal plane graphite electrode. The formation of dioxygen was identified using both RRDE techniques and a Clark electrode, whereas no deposit was observed by EQCM tech-

niques. After transferring the used electrode to an electrolyte solution deprived of catalyst, no catalytic activity was observed, confirming that no surface adsorption of active catalytic material had taken place.

The complex $[IrCp^*(Me_2NHC)(OH)_2]$ (**5**, Me_2NHC = N-dimethylimidazolin-2-ylidene) does form a surface deposit upon oxidation, which starts at 1.3 V *versus* RHE at pH 1.[22] The formation of dioxygen could be detected above 1.55 V *versus* RHE, while the presence of CO_2, a product of ligand degradation, was not observed.[23] *Ex situ* X-ray photoelectron spectroscopy showed the formed surface deposit does not contain large aggregates of iridium oxide and appears to consist of mononuclear molecular Ir centers.[22] *In situ* Raman spectroscopy illustrated the presence of a μ-oxo dimer in the reaction mixture under oxidative conditions, similar to what has been reported in the case of **4** by Crabtree and coworkers.[21]

The anionic complex $[IrCl_3(picolinate)(HOMe)]^-$ (**6**) displays a very long incubation time before it becomes active in the water oxidation reaction.[24] During this activation time, iridium oxide is formed on the electrode surface which is the true catalytic species during catalysis.

These different studies show that the role of the complementary ligands in iridium complexes have a dramatic effect on the homogeneity, the structure and the potential activity of the active species. The outstanding activity and longevity of the complexes **1** and **2** in the presence of sacrificial reagents prompted us to study these systems by electrochemical techniques and compare their results with the benchmark systems above.[13]

2.2 Experimental

2.2.1 Electrochemical methods

All experiments were performed on an Autolab PGSTAT 128N potentiostat. The experiments were carried out in a 25 ml glass cell in a three-electrode setup, using a gold working electrode (WE) (99.999%, Alfa Aesar). A gold wire (99.99%, Alfa Aesar) acted as counter electrode and the experiments were performed *versus* the reversible hydrogen electrode (RHE). The electrochemical cell was boiled twice in Millipore MilliQ water (>18.2 MΩ cm resistivity) prior to the experiment. The gold WE consisted of a disc (0.05 cm^2 geometrical surface area) and was used in a hanging meniscus configuration. The WE was cleaned by applying 10 V between the WE and a

graphite counter electrode for 30 s in a 10% H_2SO_4 (Sigma Aldrich 95%, ACS reagent) solution. This was followed by dipping the WE in a 6 M HCl (VWR chemicals 37%, Normapur) solution for 20 s. The electrode was flame annealed, followed by electrochemical polishing in 0.1 M $HClO_4$ (Merck, Suprapur), scanning between 0 and 1.75 V versus RHE for 200 cycles at 1 V s^{-1}. The electrolyte consisted of 0.1 M $HClO_4$ (Merck Suprapur, used as received) in Millipore MilliQ water (>18.2 MΩ cm resistivity) in which complex **1** or **2** was dissolved to make 0.5 mM solutions. The complexes were synthesised and characterized in the Albrecht group and made available for this investigation.[13] The electrochemical cell was purged with argon (Linde, 6.0) for at least 15 minutes prior to experiments.

2.2.2 OLEMS setup

The online electrochemical mass spectrometry (OLEMS) setup consisted of a hydrophobic porous tip (Kel-F with a Teflon plug), brought in close proximity to the WE. The gaseous products formed during electrochemistry were transferred through the tip into the mass spectrometer (Pfeiffer QMS200). An Ivium A06075 potentiostat was used to perform the electrochemical experiments.

A quadrupole mass spectrometer works on the principle of measuring the current of the ionized products impinging on the detector. The ion current of the mass spectrometer observed in the OLEMS is dependent on different factors:

- The rate of gas formation on the electrode surface
- The distance between the working electrode and the Teflon tip
- The rate of diffusion of the gas through the electrolyte
- The diffusion rate through the Teflon tip
- The ionizability of the gas

The distance between the working electrode and the tip is independent of the gas evolved, but might differ over different experiments. The gases in a quadrupole mass spectrometer are detected by means of ionization of the gaseous molecules. The ionizability of the gases differs between different molecules. The sensitivity for common gases are well-tabulated for use in ionizing pressure gauges, relative to nitrogen gas. Dioxygen has a sensitivity factor of 0.9, while carbon dioxide has a sensitivity factor of 0.7 versus N_2.[25] Thus the sensor is 1.25 times more

sensitive for dioxygen than for carbon dioxide. The diffusion of gases through the electrolyte solution is similar, 1.67×10^{-5} cm^2 s^{-1} for CO_2 and 2.01×10^{-5} cm^2 s^{-1} for O_2.[26] The distance between the electrode and the tip is small (10-100 μm) and should not influence the sensitivity for different gases significantly. Since the distance between the tip and the working electrode will differ over different experiments, the absolute ion current measured between different experiments cannot be compared and therefore all mass spectrometry data are displayed unitless.

2.2.3 Data processing in OLEMS

In an OLEMS experiment combined with cyclic voltammetry, two different datafiles are produced: electrochemical data and the mass spectrometer (MS) data. The MS data does not include the potential applied in a cyclic voltammetry. The potential can be generated manually by noting the start cycle in the MS data and using the scan rate of the CV. It has been observed that over very long experiments,the potential can drift due to discrepancies in the scan rate of the potentiostat. A method to generate the potential based on the start- and endtime of the different cycles is developed and used to couple the applied potential to the MS data.

In the MS data, the scans are separated and the time in each scan normalized. The potential is then generated using Equation 2.1,

$$E(t) = \frac{E_l - E_h}{\pi} \times \sin^{-1}\left(\sin\left((-)2\pi \times t + \frac{\pi}{2} + \pi\frac{E_s - E_l}{E_h - E_l}\right)\right) + E_l + \frac{E_h - E_l}{2} \quad (2.1)$$

where E_l and E_h are the lower and upper limits of the CV, E_s is the starting potential and t is the normalized time. The minus sign between parenthesis is only added if the scan starts in the negative direction and $E_s \neq E_l$ or $E_s \neq E_h$.

The first term ($\frac{E_l - E_h}{\pi}$) changes the amplitude of the sinusoidal wave to the vertex potential of the cyclic voltammogram. The last part ($E_l + \frac{E_h - E_l}{2}$) moves the equilibrium to the middle of the two vertices. The central part of Equation 2.1 ($\frac{\pi}{2} + \pi\frac{E_s - E_l}{E_h - E_l}$) moves the period of the sinusoidal wave to the starting potential of the experiment.

2.2.4 EQCM setup

The electrochemical quartz crystal microbalance consisted of a PEEK cell purchased from Autolab. The cell was deoxygenated with Ar (Linde, 6.0) prior to experiment. A gold working electrode (0.35 cm^{-2} geometric surface area and 0.39 cm^2 real surface area) on a quartz crystal was used as received. A gold counter electrode was used and the experiments were measured *versus* the reversible hydrogen electrode (RHE). The RHE consisted of a Pt wire embedded in glass. The gas outlet of the electrode was connected to a bubbler. This enabled the H_2 gas to remain at the electrode during experiments without the need to bubble hydrogen. Bubbling hydrogen gas at the reference electrode during the experiment can result in a high noise in Δf during experiments. Cyclic voltammetry were performed between 1.2 and 2.0 V *versus* RHE at pre-oxidized electrodes in 0.1 M $HClO_4$ at 10 mV s^{-1}. Chronoamperometry was performed at 1.7 and 1.8 V for 15 minutes.

The sensitivity coefficient of the quartz crystal (c_f) was determined by deposition of $Pb(NO_3)_2$. An electrolyte solution containing 10 mM $Pb(NO_3)_2$ and 0.1 M $HClO_4$ was prepared. Cyclic voltammetry at 100 mV s^{-1} gave the relationship between the Δf and the amount of Pb deposited onto the electrode, calculated from the current observed during cyclic voltammetry, assuming 100% faradaic efficiency towards Pb deposition. The sensitivity coefficient was determined to be 1.26×10^{-8} g cm^{-2} Hz^{-1} (Figure 2.3).

2.2.5 XPS

The XPS measurements were carried out with a Thermo Scientific K-Alpha, equipped with a monochromatic small-spot X-ray source and a 180° double focusing hemispherical analyzer with a 128-channel detector. Spectra were obtained using an aluminium anode (Al Kα = 1486.6 eV) operating at 72 W and a spot size of 400µm. Survey scans were measured at a constant pass energy of 200 eV and region scans at 50 eV. The background pressure was 2×10^{-8} mbar and during measurement 4×10^{-7} mbar argon because of charge compensation.

Samples for XPS were prepared by chronoamperometry in 0.1 M $HClO_4$ at pH 1 with 0.5 mM solutions of **1**, using EQCM gold working electrodes at 1.8 V *versus* RHE for 1, 2, 5 and 10 minutes with a gold counter electrode.

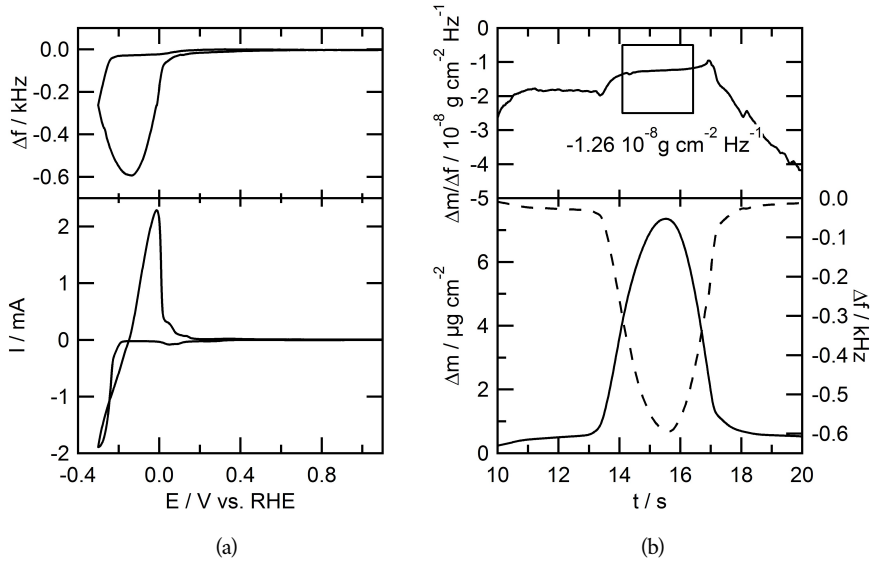

Figure 2.3: Calibration of the EQCM by bulk deposition of $PbNO_3$. a) The bottom panel shows the cyclic voltammogram of a 10 mM $PbNO_3$ solution in 0.1 M $HClO_4$ electrolyte solution at 100 mV s^{-1} on a gold electrode (1.5 cm^2 geometric surface area). The top panel shows the corresponding frequency change measured during the cyclic voltammetry. b) The bottom panel shows the frequency (dotted line) and mass change (solid line) between 0.1 to -0.3 and back to 0.1 V in time. The mass change is calculated from the current assuming 100% faradaic efficiency for the deposition of Pb . The top panel shows the sensitivity coefficient c_f which is averaged over the data points highlighted by the box.

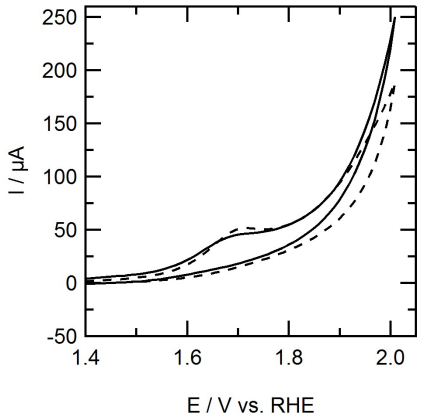

Figure 2.4: Fifth scan of cyclic voltammetry on a Au electrode (0.050 cm^2 in 0.1 M $HClO_4$ electrolyte solution) with 0.5 mM of **1** (solid line) and **2** (dotted line) in solution at pH 1 at 100 mV s^{-1}. The oxidative regime of the fifth scan between 1.4 and 2.0 V *versus* RHE is displayed.

2.2.6 XAS

X-ray absorption spectra were collected at the iridium L_3-edge (11215 eV) on the EXAFS station (BM26A) of the Dutch-Belgian beamline (DUBBLE)[27] at the European Synchrotron Radiation Facility (ESRF) in Grenoble, France. The solid benchmark materials were diluted with boron nitride and measured as pressed pellets in the transmission mode; 2 scans were averaged together to improve the signal-to-noise ratio. The samples were also recorded in the transmission mode and 6 - 8 scans were averaged. The EXAFS spectra were processed using Viper[28] and simulations were performed in EXCURVE.[29, 30] Samples were prepared by oxidizing graphite electrodes at 2.0 V *versus* RHE for 10 minutes in 1 mM solutions of **5** in 0.1 M $HClO_4$.

2.3 Results

The redox processes occurring in the presence of complexes **1** and **2** were investigated with cyclic voltammetry. In this study the working electrode is in a hanging meniscus configuration, meaning the electrode approaches the electrolyte from the top. Any solid material formed in proximity of the electrode which is not adsorbed will precipitate into the electrolyte and sink to the bottom

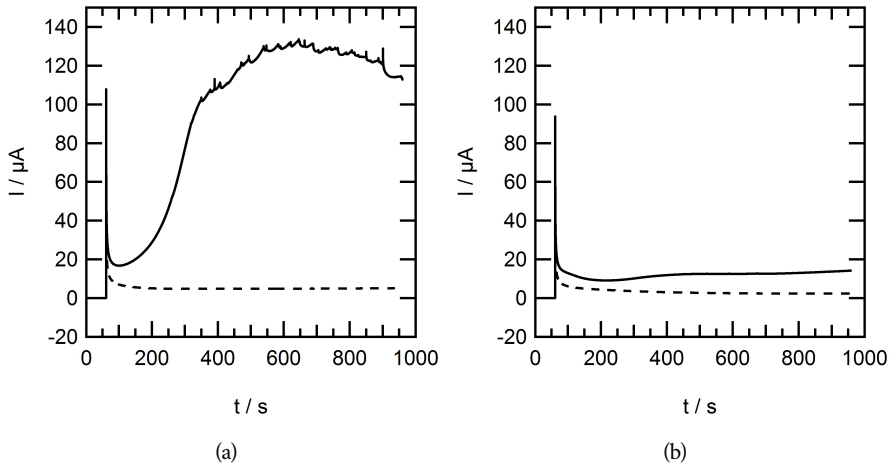

Figure 2.5: Chronoamperometry of 0.5 mM solutions of a) complex **1** and b) complex **1** at a gold electrode while applying 1.7 V (dotted line) and 1.8 V (solid line) *versus* RHE in a 0.1 M $HClO_4$ electrolyte solution. The lower potential region (0.7 to 1.4 V) is omitted for clarity.

of the electrochemical cell. The oxidation of gold, in absence of catalyst observed between 1.2 and 1.6 V, is not visible in the cyclic voltammograms. The reduction of the formed gold oxide is observed between 1.2 and 1.0 V, which is typical for a gold electrode in $HClO_4$ solution. Cyclic voltammetry of 0.5 mM solutions of **1** and **2** at a gold working electrode in 0.1 M $HClO_4$ was performed for 5 scans at 100 mV s^{-1} between 0.7 and 2.0 V *versus* RHE (fifth scan displayed in Figure 2.4). In both the cyclic voltammograms of **1** and **2**, an oxidative peak is observed at 1.7 V. This oxidative peak is most likely due to redox events of the complexes, but in part may also be caused by further oxidation of the gold working electrode.[31–42] Between 1.8 and 2.0 V, both complexes show a catalytic current which increases with the applied potential. With 220 µA *versus* 190 µA at 2 V *versus* RHE, the maximum current observed with complex **1** present in solution is higher than with complex **2** in solution. The activity of complex **1** increases from 180 to 220 µA at 2.0 V over 5 consecutive scans, whereas in the cyclic voltammogram with complex **2** in solution identical currents over 5 scans are observed. The oxidative wave at 1.7 V is present in all scans for both complexes.

Chronoamperometry was performed at 1.7 V to investigate the nature of the oxidation event

and at 1.8 V to investigate the activity of the complexes for water oxidation in a hanging meniscus configuration (Figure 2.5). At an applied potential of 1.7 V *versus* RHE little current is observed for both complexes (< 5 μA), indicating that little to no water oxidation activity takes place. At 1.8 V both complexes show an increase in current over time. In chronoamperometry experiments with complex **1** present in the electrolyte solution a minimum current after 40 seconds of amperometry is observed. Between 40 and 300 seconds the current increases, which is probably due to the activation of the complex. After 300 seconds the current stabilizes around 120 μA. For complex **2** the current goes through a minimum after 120 seconds of amperometry. An increase in current observed, reaching a final current of 14 μA after 900 seconds of amperometry. With complex **2** in solution, less current is observed than with complex **1** in the time frame of the experiment, which is in agreement with the maximum activity of both complexes at 2.0 V in cyclic voltammetry. The significant increase in current over time suggests that activation of the catalyst has taken place, but may also point to formation of a surface deposit. This is further investigated with EQCM.

In these EQCM experiments, a quartz crystal with a 200 nm layer of Au (0.35 cm^2 geometric surface area) is oscillated at 6 MHz. The oscillation frequency of the quartz crystal is directly related to the mass of the crystal, including the Au layer. This allows one to accurately determine the mass changes of the electrode by recording the frequency of oscillation during an electrochemistry experiment. It is important to note here that beside small changes in mass, also changes in the hydrophobicity have a strong effect on the oscillation frequency. Local changes in hydrophobicity are to be expected when the solution becomes saturated in dioxygen and gas bubbles start to form.[43]

In the cyclic voltammogram in the EQCM setup, the working electrode is situated at the bottom of the electrochemical cell. This is in contrast to the experiments described above, where the working electrode was used in a hanging meniscus configuration. One of the drawbacks of the use of gold electrodes in general and specifically in combination with the EQCM is gold oxidation and reduction chemistry, which may influence the electrochemical behavior of the complexes under study. In particular the oxidation of gold has a dramatic effect on the frequency of the quartz crystal. Upon prolonged cycling in $HClO_4$ electrolyte, this might lead to the destruction of the EQCM electrode altogether. This can be circumvented by keeping the potential either above

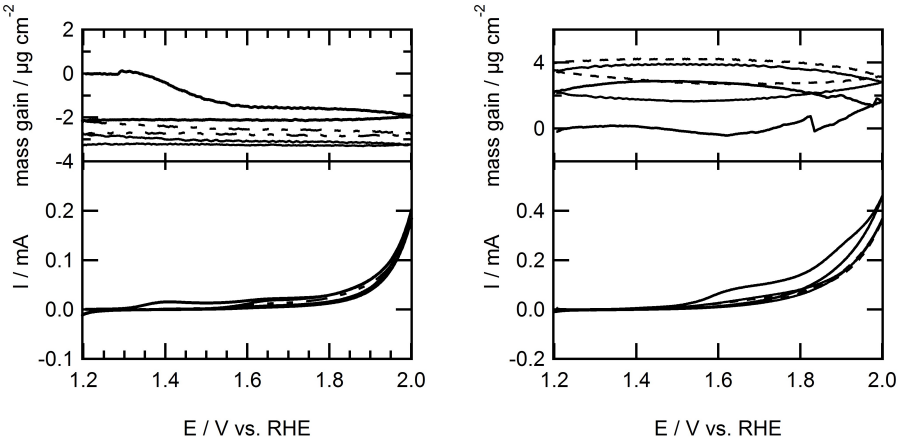

Figure 2.6: Cyclic voltammograms of 0.5 mM solutions of **1** (a) and **2** (b) in 0.1 M $HClO_4$ at 10 mV s^{-1} (bottom) and the potential-dependent mass gain, calculated from the changes of oscillation frequency of the quartz crystal-working electrode assembly.

or below 1.2 V *versus* RHE during an experiment, limiting the potential window for investigation.

There are several examples where EQCM is used to investigate the formation of a surface deposit. While oxidizing water at a gold electrode using **5**, a deposition is formed at the gold electrode. [22] The oxidation was performed in 0.1 M Na_2SO_4 electrolyte between 1.25 and 2.1 *versus* RHE at 10 mV s^{-1}. At pH 1 a mass increase of 3 µg cm^{-2} was reported over the course of three scans. This surface deposit is unstable in electrolytes without any complex present. Also in cyclic voltammetry experiments at low potential, a decrease in mass is observed.[22] Crabtree *et al* investigated several iridium-based complexes using EQCM as well.[21, 44] The complex $[Ir(Cp^*)(OH_2)_3]SO_4$ (**3**) forms the so-called blue layer on the electrode surface, with a total mass increase on the quartz crystal of 0.75 µg. The blue layer does not desorb from the electrode surface in absence of $[Ir(Cp^*)(OH_2)_3]SO_4$ in the electrolyte solution. In contrast to **3**, the complex $[Ir(Cp^*)(pyalc)(CF_3COO)]$ (**4**) does not show any deposit at all, suggesting that the active species in the latter is a truly homogeneous catalyst.

The cyclic voltammogram of complex **1** shows an oxidation event between 1.3 and 1.5 with

a peak current of 15 μA in the first scan in the EQCM configuration at a gold electrode in 0.1 M $HClO_4$ electrolyte at 10 mV s^{-1}. A second oxidative peak is observed at 1.65 V, with a peak current of 21 μA. This is followed by a faradaic wave, starting at 1.75 V and reaching a maximum current of 185 μA at 2.0 V. In the backward scan, a reductive wave is observed between 1.3 and 1.2 V, reaching a maximum current of -10 μA at 1.2 V. In the second and third scan, the first oxidation wave between 1.3 and 1.5 V is no longer observed and the peak current of the oxidation event at 1.65 V decreases in current. The catalytic current increases with each consecutive scan. At 2.0 V, the current is 180 μA in the second scan and 200 μA in the third scan. The QCM data appears to point to a decrease in mass of the electrode assembly over the course of the experiment, which is most likely to due hydrophobicity effects by formation of oxygen bubbles.

In the first scan of the cyclic voltammogram of complex **2**, an oxidation event is observed starting at 1.5 V with a peak current of current of 85 μA at 1.65 V. The oxidative peak is followed by a faradaic wave that increases from 1.75 to 2.0 V to a maximum current of 460 μA. In the backward scan a reductive wave is observed between 1.25 and 1.2 V. In the second and third scan the oxidative peak at 1.6 V is no longer visible and the current of the catalytic wave decreases to roughly 370 μA. The reductive wave between 1.25 and 1.2 V is still visible in the second and third backward scan. The QCM response corresponding to the cyclic voltammogram in the first scan shows an increase in mass between 1.6 to 2.0 V, which keeps increasing in the backward scan to 1.5 V leading to a total mass gain of 3.3 μg cm^{-2}. A subsequent decrease in mass of 1.2 μg cm^{-2} is observed between 1.5 and 1.2 V and at the start of the second scan up to 1.55 V. At 1.55 V the mass of the electrode starts increasing again and at 1.75 V in the backward scan it stabilizes at a mass gain of 2.1 μg cm^{-2}. The mass decreases again at 1.35 V in the backward scan until 1.55 V is reached in the forward scan in the third cycle with a total decrease of 1.2 μg cm^{-2}. Between 1.8 V in the forward scan and 1.7 V in the backward scan, the mass increases another 1.3 μg cm^{-2}. Finally, between 1.4 and 1.2 V of the third backward scan, a small decrease of 0.2 μg cm^{-2} is observed, leading to a total mass increase of 3.8 μg cm^{-2} over three scans.

Both complex **1** and **2** form a deposit on the electrode surface under chronoamperometric conditions at 1.8 V *versus* RHE (Figure 2.7). The formation of the surface deposit is accompanied with an increase in current. Accumulation of material on the working electrode starts the moment 1.8 V is being applied. In case of a 0.5 mM solution of complex **1** the total amount of

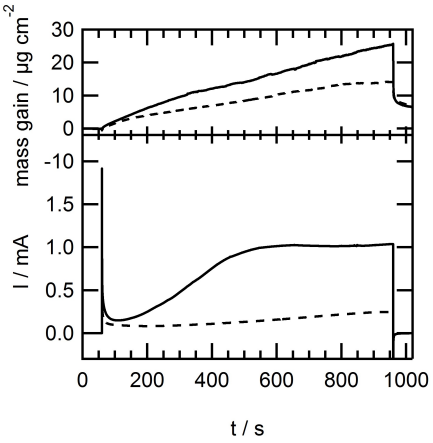

Figure 2.7: Bottom: chronoamperometry at 1.8 V at a Au electrode (0.39 cm^2) in a 0.5 mM solution complex **1** (solid line) or **2** (dotted line) and 0.1 M $HClO_4$. Top: The corresponding mass change as calculated from the frequency change recorded by EQCM.

material deposited after 15 minutes of amperometry is 10 µg cm^{-2}. For an equimolar solution of complex **2** less deposition is observed: 5.5 µg cm^{-2}. The chronoamperometry at 1.8 V of complex **1** shows an increase in current, until after 500 seconds of oxidation, the current stabilizes at 1 mA. An increase in current is observed upon oxidation of complex **2** as well, but it does not stabilize and after 15 minutes of oxidation, only 250 µA current is obtained. This suggests that complex **1** is activated quicker than complex **2** at a gold electrode in 0.1 M $HClO_4$ at 1.8 V. After oxidation, the potential is returned to 0.7 V, resulting in an apparent mass loss of approximately 50%, which may be due to changes in the hydrophobicity of the local electrolyte. Another explanation could be the loss of material from the electrode, which was observed previously with very similar IrCp* complexes including **5**.[21, 22]

To investigate whether the complexes or the surface deposits are truly active water oxidation catalysts, the gaseous products are analyzed by OLEMS. Apart from the formation of dioxygen, formation of CO_2 is to be expected in case the ligands (*e.g.* Cp*, see Figure 2.2) are oxidized during catalysis. Linear sweep voltammetry in combination with mass spectrometry shows the formation of both oxygen and carbon dioxide for both complexes, as is displayed in Figure 2.8.

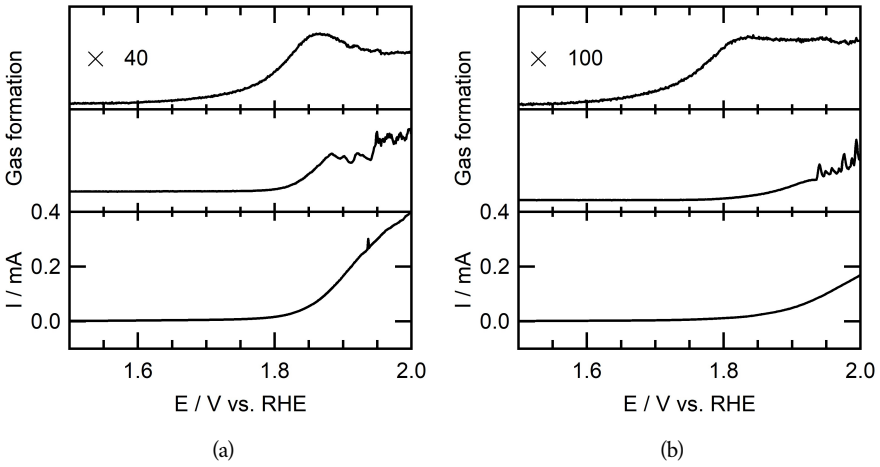

Figure 2.8: a) Linear sweep voltammogram of a 0.5 mM solution of **1** (bottom panel) in 0.1 M $HClO_4$ at 1 mV s^{-1} while tracking the production of CO_2 (top panel) and O_2 (middle panel). The top panel has been magnified 30 times for clarity. b) Cyclic voltammogram of a 0.5 mM solution of **2** (bottom panel) in 0.1 M $HClO_4$ at 1 mV s^{-1} while tracking the production of CO_2 (top panel) and O_2 (middle panel) in 0.1 M $HClO_4$. The top panel has been magnified 20 times for clarity.

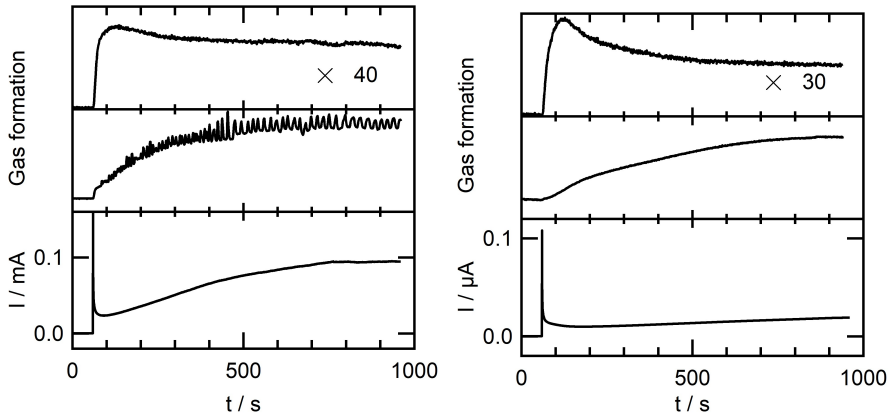

Figure 2.9: a) Chronoamperometry at 1.8 V *versus* RHE of complex **1** (bottom panel) while tracking the production of CO_2 (top panel) and O_2 (middle panel) in 0.1 M $HClO_4$. b) Chronoamperometry at 1.8 V *versus* RHE of complex **2** (bottom panel) while tracking the production of CO_2 (top panel) and O_2 (middle panel) in 0.1 M $HClO_4$.

With complex **1** in solution, carbon dioxide formation starts at 1.6 V . A maximum in rate of carbon dioxide formation is observed at 1.85 V, after which it decreases and eventually stabilizes at 1.95 V. Oxygen formation starts at 1.8 V which is at a significantly higher potential than the first burst of CO_2. At 1.88 V, the oxygen mass trace starts spiking, which points to the formation of gas bubbles at the surface of the electrode. The observed ion current for oxygen is two orders of magnitude higher than the ion current of carbon dioxide.

Complex **2** produces carbon dioxide beyond 1.55 V as is observed from the linear sweep voltammogram (Figure 2.8b). Evolution of oxygen starts at 1.8 V. In the oxygen trace, the spiky signal associated with bubble formation is observed beyond 1.95 V. The ion current for oxygen in this case is approximately 40 times higher than the ion current for CO_2.

In situ mass spectrometry in combination with chronoamperometry shows that complex **1** produces large amounts of dioxygen at the moment when an oxidizing potential is applied, whereas the activation of complex **2** to an active species takes a considerable longer reaction time (see Figure 2.9). The observed current in chronoamperometry with **1** in solution has a minimum

of 23 μA after 30 s and increases to 94 μA after 700 s of oxidation at 1.8 V where it stabilizes. In the chronoamperometry of **2**, the current goes through a minimum current of 9.9 μA after 120 seconds of oxidation and from there on increases up to 19 μA until the experiment was stopped at 15 minutes. The oxygen traces follow the current profiles of **1** and **2** exactly, apart from the spikes due to bubble formation in the case of **1**. Whereas evolution of dioxygen is sluggish at first in the case of complex **2**, an immediate burst of CO_2 is detected for both complex **1** and **2** upon applying a 1.8 V potential. After 70 seconds, the CO_2 evolution rate stabilizes upon oxidation of complex **1**. Complex **2** also evolves CO_2, with a peak at 60 seconds. The CO_2 evolution rate slowly decays and stabilizes after 400 seconds. The ion current observed for CO_2 is approximately 40 times lower than the O_2 formation, both in case of complex **1** and complex **2**.

In order to further investigate the structure of the active surface deposit, X-ray Photoelectron Spectroscopy (XPS) was measured of the gold electrode *ex situ* after water oxidation in the presence of complex **1**. Water oxidation was performed by amperometry at 1.8 V *versus* RHE in a 0.1 M $HClO_4$ and 0.5 mM solution of complex **1**. The electrode was taken out of the electrolyte and rinsed carefully with water. Different oxidation times from 1 to 10 minutes were used to track the evolution of the deposit.

Since XPS is a surface sensitive technique, the intensity of the Au XPS peaks should decrease as more material is deposited on the electrode surface (Figure 2.10a). The Au 4f peak is observed at 84.1 eV. This peak indeed decreases in intensity with increasing oxidation time, confirming that a layer of material has covered the gold electrode during the deposition experiment. The gold peak decreased to 10 percent of the initial intensity after 1 minute of oxidation.

The binding energy of 4f electrons in iridium is expected between 60.5 and 61 eV for metallic Ir, and expected up to 65 eV for highly oxidized iridium species such as $KIrCl_5NO$.[45] The binding energy of the 4f electrons in the molecular water oxidation complex **4** is found at 62.4 eV. [46, 47] The XPS spectrum for the gold electrode with the oxidized complex **1** shows a peak at 62.4 eV (Figure 2.10b. The intensity of the XPS sample correlates well with the oxidation time and amount of material deposited on the electrode.

In our group, the complex $[IrCl_3(pic)(MeOH)]^-$ (**6** - pic = picolinate) was determined to be a pre-catalyst for water oxidation. [24] The complex was degraded upon oxidation and an activated process is observed. An XPS analysis of the deposition after water oxidation catalysis shows the

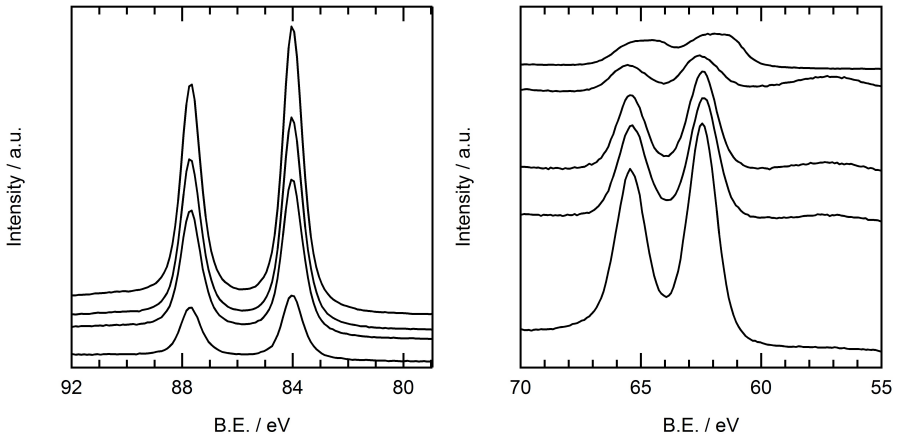

Figure 2.10: a) X-ray photoelectron spectra in the Au 4f region. From top to bottom the surface deposit on the gold electrode after 1, 3, 5 and 10 minutes of oxidation at 1.8 V *versus* RHE is displayed. b) X-ray photoelectron spectra in the Ir 4f region. The top trace is the powdered form of **1**, the rest from top to bottom is the surface deposit on the gold electrode after 1, 3, 5 and 10 minutes of oxidation at 1.8 V *versus* RHE.

Ir 4f electrons have a binding energy of 62.0 V. This is close to the values of benchmark Ir_2O_3, which are found at roughly 61.8 eV.

The surface deposit formed when complex **5** is oxidized has also been investigated using XPS.[22] The XPS spectrum shows the binding energy of the Ir 4f electrons is 62.2 eV, which is somewhat lower than was observed for activated **1** and activated **4**. Verification whether the deposit of complex **5** contains molecular structures, or is the path to formation of iridium oxide was obtained by extended X-ray absorption fine structure (EXAFS) analysis.

In EXAFS, among others the distance between the iridium center and the atoms in its direct environment can be investigated. The bond length between the iridium and its neighbors is indicative of the oxidation state of iridium and the type of atom that is present in the first coordination sphere. For an Ir-C bond, a longer bond length is expected compared to an Ir-O bond. In this investigation, the surface deposits of **5** were investigated and compared to the parent complex and benchmark IrO_2, as displayed in Figure 2.11 and Table 2.1. Complex **5** (1 mM in 0.1 M $HClO_4$ electrolyte) was oxidized at graphite foil at a range of potentials: 1.1 V, 1.3 V, 1.5 V, 1.7 V, 1.9 V and 2.0 V *versus* RHE for 5 minutes. In the parent complex, the measured bond length between the Ir center and its closest neighbor is 2.08 Å. The Ir-O bond length in IrO_2 is determined to be 1.96 Å. Oxidizing complex **5** at potentials between 1.1 and 1.5 V bond lengths between 2.04 and 2.11 Å are observed. Oxidizing the complex between 1.5 and 2.0 V decreases the bond length to 2.00-2.04 Å. The bond lengths found in case of **5** is still higher than the bond length found for IrO_2. In contrast to IrO_2, no signs pointing to short iridium-iridium distances have been observed in case of oxidized **5**.

2.4 Discussion

In contrast to electrochemical oxidation of **4**, deposits are formed on the electrode surface upon oxidation of complexes **1** and **2**. Whereas no deposition appears to be formed in case of **1** in cyclic voltammetry mode (Figure 2.6), a considerable large change in frequency in EQCM is observed compared to complex **2** in amperometry mode. It is not straightforward to interpret these data. The changes in frequency appear to be strongly related to the precise reaction conditions as well as the catalyst structure in ways we do not yet fully understand.[44] Moreover changes in the local hydrophobicity caused by bubble formation result in QCM frequency changes as well. This

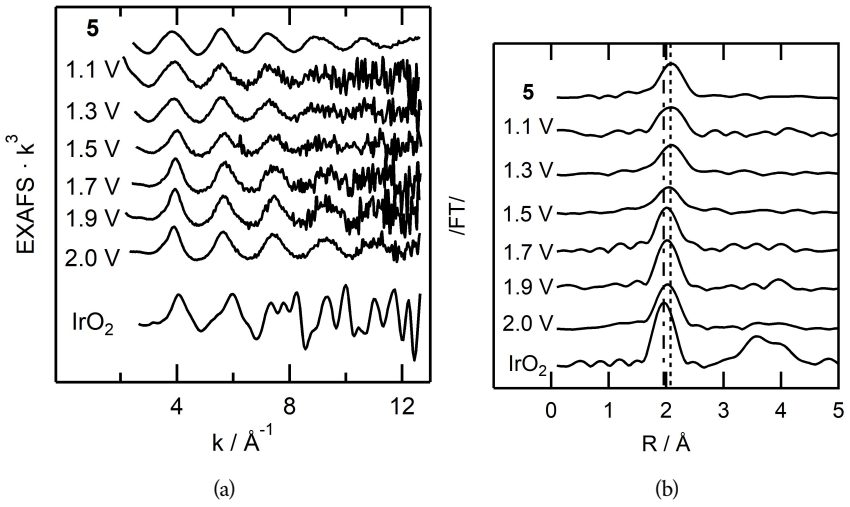

Figure 2.11: a) k^3 weighted iridium L_3 edge EXAFS and b) the modulus of the corresponding phase-corrected FT of 2 reference compounds and graphite electrodes exposed to different oxidizing potentials. From top to bottom: **5**, electrode oxidized at 1.1 V, 1.3 V, 1.5 V, 1.7 V, 1.9 V and 2.0 V, and benchmark IrO_2. The grey line and dotted grey line in b show the peak position of **5** and IrO_2 respectively.

Table 2.1: *Single shell simulations with C (carbon) or O (oxygen) for selected reference compounds and carbon electrodes exposed to certain potentials. The best fit index (C or O) is highlighted in bold.*

	C			O		
	Threshold energy(eV)	Number of atoms@distance (Å) and Debye–Waller factor ($2\sigma^2$, Å^2)	Fit index with k^3-weighting ($\times 10^3$)	Threshold energy(eV)	Number of atoms@distance (Å) and Debye–Waller factor ($2\sigma^2$, Å^2)	Fit index with k^3-weighting ($\times 10^3$)
5	-10.5607	5.7@2.147 (0.007)	**0.4903**	-14.6284	4.1@2.110 (0.009)	0.5555
1.1 V	-16.8836	6.8@2.139 (0.016)	**1.9858**	-19.6258	5.0@2.090 (0.019)	2.1008
1.3 V	-9.1949	5.9@2.146 (0.011)	**1.0433**	-12.1444	4.5@2.101 (0.014)	1.0929
1.5 V	-7.99290	5.0@2.100 (0.010)	**1.3133**	-10.597	4.0@2.053 (0.015)	1.3161
1.7 V	-7.3754	5.7@2.068 (0.004)	1.3189	-11.095	4.4@2.031 (0.015)	**1.3000**
1.9 V	-11.1800	6.1@2.075 (0.003)	1.2304	-15.147	4.6@2.039 (0.005)	**1.1833**
2.0 V	-9.08911	6.1@2.087 (0.005)	0.5581	-12.6264	4.5@2.049 (0.007)	**0.4625**
IrO_2	7.26908	6.6@2.010 (0.002)	3.2154	-12.1225	4.5@1.976 (0.014)	**3.3055**

may also explain the observed currents do not fully correlate with the amount of deposition on the electrode, albeit Crabtree *et al.* in case of the blue layer formed by the oxidation of **3** already showed that only part of the iridium sites in such an arrangement is electrochemically active in water oxidation catalysis.[44] Over the entire comparison, complex **1** does show a considerable higher current compared to complex **2**, which is accompanied by oxygen bubble formation - clearly visible in Figures 2.8 and 2.9 - and saturation effects. The OLEMS experiment in amperometry mode clearly suggests that complex **1** forms a highly active species for the oxygen evolution reaction much more rapidly than complex **2** This may be due to steric effects of the OEt moiety on the triazolylidene ligand. Possibly a dimeric structure as has been characterized in case of **4** and observed in the case of complex **5** is the active species. Alternatively one can imagine that complex **1** is a good catalyst itself, whereas complex **2** is too sterically hindered for fast turnovers until the Cp* has reacted away.

It is interesting to note that the iridium signals in the *ex situ* XPS spectra of the *ex situ* deposit obtained by oxidation of **1** matches very well with the μ-oxo bridged iridium(IV) dimer obtained in the group of Crabtree upon oxidation of **4**. Although the oxidation state of iridium in IrO_2 is also +IV, the signal for IrO_2 is found at a significant lower binding energy, allowing one to distinguish between molecular iridium(IV) species and iridium(IV) present in iridium oxide. In light of these binding energies very lengthy incubation times and the presence of redox waves that are typical for iridium oxide, our group has previously assigned the active species in case of complex **6** to iridium oxide. In term of XPS spectroscopy, deposits of complex **5** lie somewhat between those of **6** and **1**.

In EXAFS, the short binding distance between iridium and its first coordination shell of 1.96 Å recorded in case of IrO_2 gives a clear benchmark for the formation of IrO_2. The surface deposits of **5** oxidized at different potentials show clearly that the bond length in all adsorbed complexes is considerably longer (between 2.0 and 2.08 Å). Although the average bond length reduces upon an increase of the applied potential, this means complex **5** does produce larger aggregates of IrO_2 within the time frames wherein the experiments have been carried out. Between 1.1 and 1.5 V, the bond length is more in line with an Ir-C bond, whereas between 1.7 and 2.0 V the bond length decreases and modeling of the complex points more to displacement of carbon for oxygen in the first coordination sphere. This suggests that the complex does change structurally

during water oxidation, yet it is unclear what is the exact active species during water oxidation. No iridium - iridium interactions could be observed, which are very pronounced in the case of IrO_2 at higher $Å^{-1}$ Most likely the deposit of **5** is a single site molecular iridium species. The obtained EXAFS results did not allow us to distinguish between different atom-type within the coordination sphere of iridium, including powders of the precursors,[48] which refrain us from further X-ray absorption studies of *e.g.* complex **1**.

In general obtaining structure reactivity studies in the electrochemical water oxidation reaction in the presence of molecular iridium precursors has been very difficult. This study is no exception herein. It appears that every molecular iridium complex is active, with **6** being an exception, while the activity throughout an experiment appears to change continuously upon oxidation of the sample and appears to be strongly dependent on the applied reaction conditions. The choice for the Cp^* functionality, which role is most likely for that of a placeholder rather than it being directly present in the active species has not made things much easier. Only in very few cases catalytic intermediates have been identified in the reaction mixture. The μ-O bridged dimer reported by Crabtree *et al.* is an unique example,[21] whereas deposited **1** appears to have a similar electronic structure, based on XPS analysis. The large plethora of iridium catalysts for the water oxidation reaction have not led to well-defined design principles. This is in contrast to for example molecular ruthenium catalysts, for which clever proton shuttles to facilitate the water nucleophilic attack mechanism, and π-stacking strategies for binuclear oxygen-oxygen coupling reactions have been invented.[49] In case of iridium, modification of the ligands employed appear to be more useful to guide activation of the precatalyst to the true active species. In many cases this has led to formation of iridium oxide that is formed sooner or later under the catalytic conditions applied, whereas in other cases ill-defined catalytic species are formed that are categorized somewhere between a heterogeneous catalyst and a single-site species. In case of **4** this has led to a well-defined binuclear catalytic system that shows a very low onset for the water oxidation reaction at remarkable low iridium loadings. In terms of XPS analysis, it appears that the complexes **1** and **2** are relatively close to such species, albeit the electrochemistry of **1** and **2** is significantly more complex.

In the electrochemical iridium-based water oxidation reaction different types of active species can be identified (Figure 2.12). One is the formation of a well-defined molecular complex in so-

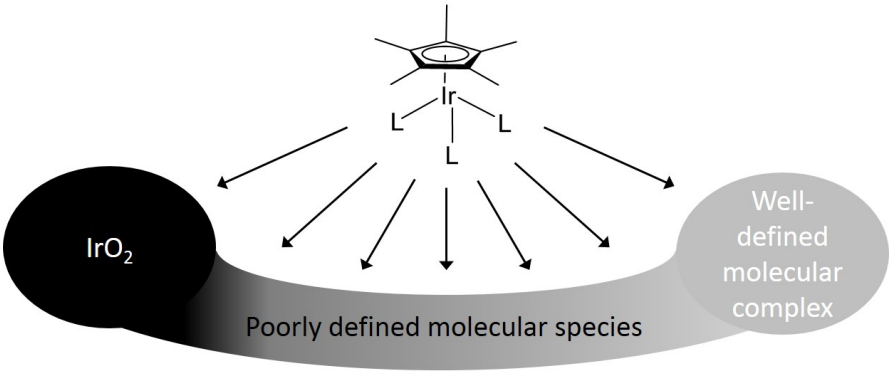

Figure 2.12: Active catalyst formation of various types of active species in the electrochemical water oxidation reaction.

lution, as was observed for complex **4**.[21] On the other side is the formation of iridium oxide as active catalyst, as was observed with the **3** and **6** precursors. In between these two extremes is a poorly defined region where the active site is a molecular complex which does form a surface deposit on the electrode. The complexes **1**, **2** and **5** are in this region. The challenge now lies in finding the prerequisites for complexes to be as much on the molecular side as possible, where ligand design already plays a large role.

The activation of pre-catalysts using the electrochemical methods presented in this work shows a different trend compared to a concerted study wherein a family of complexes including **1** an **2** was studied using the sacrificial reagent cerium ammonium nitrate.[7–13] The activation of complex **1** is faster under electrochemical conditions on all levels, but shows a remarkable slower reaction rate in the cerium ammonium nitrate driven water oxidation (1500 h^{-1} *versus* 2500 h^{-1} for complex **2**). Also it appears to activate much slower under these conditions. Where cerium ammonium nitrate and other sacrificial oxidants may be useful for the examination of intermediates and provide structural information on the catalyst, it does not always agree with results obtained with electrochemical methods. Therefore, one needs to be careful in designing catalytic experiments and in drawing conclusions from experiments in complicated reactions such as the water oxidation reaction.

2.5 Conclusions

Water oxidation has been achieved using pyridyl-triazolylidene iridium-based pre-catalysts **1** and **2**. The activation of these pre-catalysts involves the formation of a deposit on the surface of the Au working electrode.

Dioxygen and carbon dioxide formation was observed in voltammetric experiments, where the formation of CO_2 started at lower potentials than O_2. In chronoamperometric experiments, both O_2 and CO_2 formation start instantaneously upon applying an oxidizing potential in case of complex **1**, whereas the formation of O_2 is initially sluggish in case of complex **2**.

Activation of water oxidation catalysts can differ greatly with different means of oxidation. The observed trend in the cerium ammonium nitrate driven water oxidation reaction showed a remarkably different trend in activity than the electrochemical data presented here. This strongly suggests that the method of study in structure-activity relationships or structure-activation relationships do influence the results. Therefore it is best to use complementary techniques or at least apply a method of oxidation that is as close as possible to the final application.

2.6 References

(1) Bernet, L.; Lalrempuia, R.; Ghattas, W.; Mueller-Bunz, H.; Vigara, L.; Llobet, A.; Albrecht, M. *Chem. Commun.* **2011**, *47*, 8058.

(2) Gersten, S. W.; Samuels, G. J.; Meyer, T. J. *J. Am. Chem. Soc.* **1982**, *104*, 4029–4030.

(3) Wasylenko, D. J.; Ganesamoorthy, C.; Henderson, M. A.; Berlinguette, C. P. *Inorg. Chem.* **2011**, *50*, 3662–3672.

(4) Concepcion, J. J.; Jurss, J. W.; Norris, M. R.; Chen, Z.; Templeton, J. L.; Meyer, T. J. *Inorg. Chem.* **2010**, *49*, 1277–1279.

(5) Duan, L.; Bozoglian, F.; Mandal, S.; Stewart, B.; Privalov, T.; Llobet, A.; Sun, L. *Nat. Chem.* **2012**, *4*, 418–423.

(6) Zuccaccia, C.; Bellachioma, G.; Bortolini, O.; Bucci, A.; Savini, A.; Macchioni, A. *Chem. Eur. J.* **2014**, *20*, 3446–56.

(7) Lalrempuia, R.; McDaniel, N. D.; Müller-Bunz, H.; Bernhard, S.; Albrecht, M. *Angew. Chem. Int. Ed.* **2010**, *49*, 9765–9768.

(8) Petronilho, A.; Rahman, M.; Woods, J. A.; Al-Sayyed, H.; Müller-Bunz, H.; MacElroy, J. M. D.; Bernhard, S.; Albrecht, M. *Dalton T.* **2012**, *41*, 13074.

(9) Woods, J. A.; Lalrempuia, R.; Petronilho, A.; McDaniel, N. D.; Müller-Bunz, H.; Albrecht, M.; Bernhard, S. *Energ. Environ. Sci.* **2014**, *7*, 2316.

(10) Corbucci, I.; Petronilho, A.; Müller-Bunz, H.; Rocchigiani, L.; Albrecht, M.; Macchioni, A. *ACS Catal.* **2015**, *5*, 2714–2718.

(11) Navarro, M.; Li, M.; Müller-Bunz, H.; Bernhard, S.; Albrecht, M. *Chem. Eur. J.* **2016**, *22*, 6740–6745.

(12) Navarro, M.; Smith, C. A.; Li, M.; Bernhard, S.; Albrecht, M. *Chem. Eur. J.* **2018**, *24*, 6386–6398.

(13) Olivares, M.; van der Ham, C. J. M.; Li, M.; Müller-Bunz, H.; Verhoeven, M. W. G. M.; Niemantsverdriet, J. W.; Hetterscheid, D. G. H.; Bernhard, S.; Albrecht, M. *In preparation*.

(14) Hetterscheid, D. G. H.; Reek, J. N. H. *Eur. J. Inorg. Chem.* **2014**, 742–749.

(15) Wasylenko, D. J.; Ganesamoorthy, C.; Borau-Garcia, J.; Berlinguette, C. P. *Chem. Commun.* **2011**, *47*, 4249.

(16) Yoshida, M.; Masaoka, S.; Abe, J.; Sakai, K. *Chem. Asian J.* **2010**, *5*, 2369–2378.

(17) Codolà, Z.; Gómez, L.; Kleespies, S. T.; Que Jr, L.; Costas, M.; Lloret-Fillol, J. *Nat. Commun.* **2015**, *6*, 5865.

(18) Hong, D.; Murakami, M.; Yamada, Y.; Fukuzumi, S. *Energ. Environ. Sci.* **2012**, *5*, 5708–5716.

(19) Blakemore, J. D.; Schley, N. D.; Balcells, D.; Hull, J. F.; Olack, G. W.; Incarvito, C. D.; Eisenstein, O.; Brudvig, G. W.; Crabtree, R. H. *J. Am. Chem. Soc.* **2010**, *132*, 16017–16029.

(20) Blakemore, J. D.; Schley, N. D.; Olack, G. W.; Incarvito, C. D.; Brudvig, G. W.; Crabtree, R. H. *Chem. Sci.* **2011**, *2*, 94–98.

(21) Schley, N. D.; Blakemore, J. D.; Subbaiyan, N. K.; Incarvito, C. D.; D'Souza, F.; Crabtree, R. H.; Brudvig, G. W. *J. Am. Chem. Soc.* **2011**, *133*, 10473–10481.

(22) Hetterscheid, D. G. H.; van der Ham, C. J. M.; Diaz-Morales, O.; Verhoeven, M. W. G. M.; Longo, A.; Banerjee, D.; Niemantsverdriet, J. W.; Reek, J. N. H.; Feiters, M. C. *Phys. Chem. Chem. Phys.* **2016**, *18*, 10931–10940.

(23) Diaz-Morales, O.; Hersbach, T. J. P.; Hetterscheid, D. G. H.; Reek, J. N. H.; Koper, M. T. M. *J. Am. Chem. Soc.* **2014**, *136*, 10432–10439.

(24) Abril, P.; del Rio, M. P.; Tejel, C.; Verhoeven, T. W. G. M.; Niemantsverdriet, J. W.; Van der Ham, C. J. M.; Kottrup, K. G.; Hetterscheid, D. G. H. *ACS Catal.* **2016**, *6*, 7872–7875.

(25) Moore, J. H.; Davis, C. C.; Coplan, M. A.; Greer, S. C., *Building scientific apparatus: a practical guide to design and construction*, 1989, p 102.

(26) Lide, D. R., *CRC Handbook of Chemistry and Physics, 84th Edition, 2003-2004*, 2003; Vol. 53, p 2616.

(27) Nikitenko, S.; Beale, A. M.; van der Eerden, A. M. J.; Jacques, S. D. M.; Leynaud, O.; O'Brien, M. G.; Detollenaere, D.; Kaptein, R.; Weckhuysen, B. M.; Bras, W.; IUCr *J. Synchrotron Radiat.* **2008**, *15*, 632–640.

(28) Klementev, K. V. *J. Phys. D: Appl. Phys.* **2001**, *34*, 209–217.

(29) Gurman, S. J.; Binsted, N.; Ross, I. *J. Phys. C: Solid State Phys.* **1986**, *19*, 1845–1861.

(30) Gurman, S. J.; Binstedt, N.; Ross, I. *J. Phys. C: Solid State Phys.* **1984**, *17*, 143–151.

(31) Awad, M. I.; Ohsaka, T. *Journal of Power Sources* **2013**, *226*, 306–312.

(32) Burke, L. D.; O'Sullivan, J. F. *J. Electroanal. Chem.* **1990**, *285*, 195–207.

(33) Doyle, R. L.; Lyons, M. E. G. *J. Solid State Electr.* **2014**, *18*, 3271–3286.

(34) Baten, S. M. A.; Taylor, A. G.; Wilde, C. P. *Electrochim. Acta* **2008**, *53*, 6829–6834.

(35) Burke, L. D.; Lee, B. H. *J. Electroanal. Chem.* **1992**, *330*, 637–661.

(36) Burke, L. D.; Nugent, P. F. *Gold Bull.* **1997**, *30*, 43–53.

(37) Iotov, P. I.; Kalcheva, S. V. *Gold Bull.* **2001**, *34*, 95–103.

(38) Doménech-Carbó, A.; Sabaté, F.; Sabater, M. J. *J. Phys. Chem. C* **2018**, *122*, 10939–10947.

(39) Zou, S.; Burke, M. S.; Kast, M. G.; Fan, J.; Danilovic, N.; Boettcher, S. W. *Chem. Mater.* **2015**, *27*, 8011–8020.

(40) Burke, L. D.; Cunnane, V. J.; Lee, B. H. *J. Electrochem. Soc.* **1992**, *139*, 3–10.

(41) Cherevko, S.; Zeradjanin, A. R.; Topalov, A. A.; Kulyk, N.; Katsounaros, I.; Mayrhofer, K. J. J. *ChemCatChem* **2014**, *6*, 2219–2223.

(42) Klaus, S.; Trotochaud, L.; Cheng, M.-J.; Head-Gordon, M.; Bell, A. T. *ChemElectroChem* **2016**, *3*, 66–73.

(43) Hetterscheid, D. G. H. *Chem. Commun.* **2017**, *53*, 10622–10631.

(44) Blakemore, J. D.; Schley, N. D.; Kushner-Lenhoff, M. N.; Winter, A. M.; Souza, D.; Crabtree, R. H.; Brudvig, G. W. *Inorg. Chem.* **2012**, *51*, 7749–7763.

(45) Moulder, J. F.; Stickle, W. F.; Sobol, P. E.; Bomben, K. D. Handbook of X-ray Photoelectron Spectroscopy., 1995.

(46) Sharninghausen, L. S.; Sinha, S. B.; Shopov, D. Y.; Choi, B.; Mercado, B. Q.; Roy, X.; Balcells, D.; Brudvig, G. W.; Crabtree, R. H. *J. Am. Chem. Soc.* **2016**, *138*, 15917–15926.

(47) Hintermair, U.; Sheehan, S. W.; Parent, A. R.; Ess, D. H.; Richens, D. T.; Vaccaro, P. H.; Brudvig, G. W.; Crabtree, R. H. *J. Am. Chem. Soc.* **2013**, *135*, 10837–10551.

(48) Feiters, M. C.; Longo, A.; Banerjee, D.; van der Ham, C. J. M.; Hetterscheid, D. G. H. *J. Phys. Conf. Ser.* **2016**, *712*, 012059.

(49) Blakemore, J. D.; Crabtree, R. H.; Brudvig, G. W. *Chem. Rev.* **2015**, *115*, 12974–13005.